



Enhanced photocatalytic inactivation of *Escherichia coli* by a novel Z-scheme $\text{g-C}_3\text{N}_4/\text{m-Bi}_2\text{O}_4$ hybrid photocatalyst under visible light: The role of reactive oxygen species



Dehua Xia^a, Wanjun Wang^{b,*}, Ran Yin^c, Zhifeng Jiang^{a,d}, Taicheng An^b, Guiying Li^b, Huijun Zhao^{e,f}, Po Keung Wong^{a,*}

^a School of Life Sciences, The Chinese University of Hong Kong, Shatin, NT, Hong Kong SAR, China

^b Institute of Environmental Health and Pollution Control, School of Environmental Science and Engineering, Guangdong University of Technology, Guangzhou 510006, Guangdong, China

^c Department of Civil and Environmental Engineering, The Hong Kong University of Science and Technology, Clear Water Bay, Kowloon, Hong Kong SAR, China

^d Institute for Energy Research, Jiangsu University, Zhenjiang, 212013, Jiangsu, China

^e Centre for Clean Environment and Energy, Griffith School of Environment, Griffith University, Queensland 4222, Australia

^f Laboratory of Nanomaterials and Nanostructures, Institute of Solid State Physics, Chinese Academy of Sciences, Hefei 230031, Anhui, China

ARTICLE INFO

Article history:

Received 2 March 2017

Received in revised form 8 May 2017

Accepted 10 May 2017

Available online 11 May 2017

Keyword:

E. coli inactivation

$\text{g-C}_3\text{N}_4/\text{m-Bi}_2\text{O}_4$

Charge transfer

Z-scheme

Bacterial destruction

ABSTRACT

Biohazards are widely present in wastewater, and contaminated water can arouse various waterborne diseases. Therefore, effective removal of biohazards from water is a worldwide necessity. In this study, a novel all-solid-state Z-scheme $\text{g-C}_3\text{N}_4/\text{m-Bi}_2\text{O}_4$ heterojunction was constructed using a facile hydrothermal approach. Using the optimum $\text{g-C}_3\text{N}_4/\text{m-Bi}_2\text{O}_4$ (1:0.5), $6 \log_{10}$ cfu/mL of *E. coli* K-12 could be completely inactivated within 1.5 h under visible light irradiation, while only $1.2 \log_{10}$ cfu/mL and $3.2 \log_{10}$ of *E. coli* K-12 were inactivated by pure $\text{g-C}_3\text{N}_4$ and Bi_2O_4 under the same experimental conditions respectively. Emphasis was placed on identifying how the charge transfers across the $\text{g-C}_3\text{N}_4/\text{m-Bi}_2\text{O}_4$ heterojunction and a Z-scheme charge transfer mechanism was verified by reactive species trapping and quantification experiments. The Z-scheme charge separation within $\text{g-C}_3\text{N}_4/\text{m-Bi}_2\text{O}_4$ populated electrons and holes into the increased energy levels, thereby enabling one-step reduction of O_2 to H_2O_2 and facilitating more generation of holes. This greatly accelerated photocatalytic efficiency on the inactivation of *E. coli*. Moreover, microscopy images indicate that cell structures were damaged and intracellular components were leaked out during the photocatalytic inactivation process. This study suggests that the newly fabricated Z-scheme $\text{g-C}_3\text{N}_4/\text{m-Bi}_2\text{O}_4$ is a promising photocatalyst for water disinfection.

© 2017 Elsevier B.V. All rights reserved.

1. Introduction

With global climate changes and increasing populations, the shortages of fresh water require increased water recycling and reuse [1,2]. Biohazards, such as bacteria, viruses, and fungi are widely present in drinking water sources (e.g., surface water and groundwater) and pose significant health risks to human [3,4]. Unfortunately, conventional water disinfection methods, including UV irradiation or chemical disinfection using ozone and chlorine, all have some disadvantages [5–9]. For example, UV irradiation could

effectively inactivate biohazards, but the high energy consumption and operational cost limit their application [5,6]. Meanwhile, an increased dosage of chemical disinfectants is needed for the inactivation of persistent biohazards, and it will increase the formation of disinfection byproducts (DBPs) [7–9]. Moreover, a number of biohazards are naturally resistant to UV and chlorination [6]. Therefore, effectively removing biohazards from water is a challenge that has received sustained attention [10–12], and versatile new technologies are highly needed to efficiently inactivate biohazards without causing secondary pollution.

Semiconductor-based photocatalysis has been recognized as a promising technology to purify water and wastewater, including decomposing a wide array of organic contaminants, as well as inactivating pathogenic biohazards, attributed to its superior photocatalytic activity, nontoxic and stable properties [13–16].

* Corresponding authors.

E-mail addresses: wanjun.w@163.com (W. Wang), [\(P.K. Wong\)](mailto:pkwong@cuhk.edu.hk).

Therefore, the search of suitable photocatalysts has been an intensively pursued topic. Over the last few decades, the development of visible-light-driven photocatalysts has evolved from modified TiO_2 to non- TiO_2 based semiconductor materials, such as metal oxides, sulfides, oxynitrides or oxysulfides and even non-metal based graphitic carbon nitride ($\text{g-C}_3\text{N}_4$) [17–20]. Among these compounds, the simple $\text{g-C}_3\text{N}_4$ is much more promising for practical application, because it has unique advantages of simple structure, low costs, facile synthesis and easy to scale up for commercial applications [21]. Moreover, the delocalized conjugated p structures in $\text{g-C}_3\text{N}_4$ have been found to lead to rapid photo-induced charge separation and a relatively slow charge recombination [22]. Furthermore, its relatively narrow band gap originating from the tri-s-triazine units connected with planar amino groups leads to efficient light harvesting within the visible light region and electric conductivity [23]. Previous work has demonstrated that $\text{g-C}_3\text{N}_4$ could inactivate 2×10^6 cfu/mL of *E. coli* within 4-h under visible light irradiation [24].

However, the photocatalytic disinfection activity of pristine $\text{g-C}_3\text{N}_4$ is far from satisfactory with light response limited to 430 nm. To fully utilize the whole sunlight spectrum, it is important to extend the light response to longer wavelength regions. Heterojunctions formation is an effective strategy to simultaneously modulate the light absorption property and enhance the interfacial charge transportation efficiency [25,26]. For example, a heterojunction with a Z-scheme charge transfer process can efficiently separate the photogenerated electrons and holes into two photosystems through an electron mediator, helping spatially isolate the oxidation and reduction reaction sites and thus enhancing the photocatalytic activity [27,28]. Recently, a novel bismuth (Bi)-based simple oxide photocatalyst (i.e., monoclinic dibismuth tetraoxide, m- Bi_2O_4) was developed. With mixed valent states (Bi^{3+} and Bi^{5+}) and a narrow band gap of 2.0 eV, it can response to wavelength up to 620 nm. It exhibits much higher photocatalytic inactivation efficiency than some of the well investigated VLD photocatalysts, such as CdS and Bi_2O_3 , etc. [29]. Inspired by the merits of heterojunction and based on the band alignment between $\text{g-C}_3\text{N}_4$ and m- Bi_2O_4 , it is reasonable to design an all-solid state heterojunction structured $\text{g-C}_3\text{N}_4/\text{m-Bi}_2\text{O}_4$.

In this study, m- Bi_2O_4 can be modified onto $\text{g-C}_3\text{N}_4$ nanosheets by a one-pot hydrothermal method using NaBiO_3 as Bi precursor. Hence, if the $\text{g-C}_3\text{N}_4/\text{m-Bi}_2\text{O}_4$ photocatalyst follows the Z-scheme mechanism, the composite might also be an efficient photocatalyst for *E. coli* inactivation. However, to the best of our knowledge, no corresponding research has been reported, which made us focus on the actual mechanism of the $\text{g-C}_3\text{N}_4/\text{m-Bi}_2\text{O}_4$ photocatalyst. Therefore, the structure and charge transfer process of the $\text{g-C}_3\text{N}_4/\text{m-Bi}_2\text{O}_4$ heterojunction were characterized by various methods. The bacterial inactivation mechanism of the $\text{g-C}_3\text{N}_4/\text{m-Bi}_2\text{O}_4$ heterojunction structure was also deeply explored. The morphological change of *E. coli* K-12 during the photocatalytic process was also investigated to evaluate the potential of the hybrid photocatalyst to enhance bacterial inactivation.

2. Experimental section

2.1. Preparation of photocatalysts

All chemicals were purchased in analytical grade and used without further purification. To synthesize $\text{g-C}_3\text{N}_4$, a given amount of melamine was placed in a covered crucible and heated to 520 °C at a heating rate of 20 °C/min and kept at 520 °C for 4 h [30]. To synthesize m- Bi_2O_4 , a suitable amount of NaBiO_3 powder was dispersed in water and put into a 100 mL Teflon lined stainless autoclave, then heated in an oven at 160 °C for 8 h [27]. In order to modify the sur-

face of $\text{g-C}_3\text{N}_4$ with m- Bi_2O_4 , different amount of NaBiO_3 was added to react with $\text{g-C}_3\text{N}_4$ via the hydrothermal reaction at 160 °C for 8 h. The resulting mixture was centrifuged and washed for several times with deionized water (18.2 MΩ·cm). Finally, the as-obtained precipitate was dried in a vacuum drier for 24 h. The BiOBr and N- TiO_2 were prepared following the methods in References [31] and [32].

2.2. Sample characterization

UV-vis diffuse-reflectance spectra (UV-vis DRS) of the as-prepared photocatalysts were recorded on a Solid Spec-3700 DUV spectrophotometer using BaSO_4 as reference and were converted from reflection to absorption by the Kubelka-Munk method. The powder X-ray diffraction (XRD) patterns were recorded on a Bruker D8 diffractometer with monochromated $\text{Cu K}\alpha$ radiation ($\lambda = 1.5418 \text{ \AA}$). Fluorescence spectra were monitored with a fluorescence spectrophotometer (Hitachi, Model F-7000) equipped with a PC recorder. Surface electronic states were analyzed by an X-ray photoelectron spectrometer (XPS, ESCALAB MK II). The morphology of the product was characterized by a scanning electron microscopy with energy dispersive X-ray spectroscopy (FESEM-EDX, FEI, Quanta 400 FEG) and a transmission electron microscope (TEM, JEOL JSM-6700F).

2.3. Photocatalytic bacterial inactivation

E. coli K-12 was chosen as the model bacterium to evaluate the photocatalytic inactivation efficiency of the prepared photocatalysts. Bacterial cells were firstly cultured in nutrient broth at 37 °C for 16 h with shaking, and then harvested by centrifugation at 10,000 rpm for 1 min. The bacterial pellets were then washed with sterilized saline (0.9% NaCl) solution two times in a centrifuge and re-suspended in a sterilized saline solution to obtain suitable concentration of *E. coli*. Then, 20 mg of the prepared photocatalyst was added into 50 mL solution containing $6 \log_{10}$ cfu/mL of bacterial suspension. The reaction solution was stirred with a magnetic stirrer throughout the experiment. A Xenon lamp (300 W) with a UV cut-off filter ($\lambda < 400 \text{ nm}$) was used as the light source with light intensity fixed at 193 mW/cm² (light emission spectrum is shown in Fig. S1). Then, at different time intervals, aliquot samples were collected and uniformly spread on nutrient agar plates after serial dilutions using the sterilized saline solution. The plates were incubated at 37 °C for 24 h to determine the viable cell count. All the inactivation experiments were conducted in triplicate.

2.4. Photoelectrochemical experiments

As-prepared photocatalysts were dispersed in α -naphthol (0.5 wt%) solution and ground for 10 min. The resultant slurry was then blade coated on a $1 \times 1 \text{ cm}^2$ fluorine tin oxide (FTO) glass substrate with a glass slide, then the film was dried in air. Photoelectrochemical experiments were performed in a conventional three-electrode cell with a platinum plate ($1 \times 1 \text{ cm}^2$) as the counter electrode and a saturated calomel electrode (SCE) as the reference electrode on an electrochemical workstation (CHI660C, Chenhua, China). The prepared working electrode was positioned in the middle of a 0.1 M Na_2SO_4 aqueous solution with the glass side facing to the incident light.

2.5. Reactive species analysis

Nitro blue tetrazolium (NBT) at 0.025 mM was used to detect the production of $\bullet\text{O}_2^-$ through measuring the absorbance by a UV-vis spectrophotometer at 259 nm [33]. Terephthalic acid (TA) at 0.5 mM in NaOH (2 mM) solution was used to detect the formation

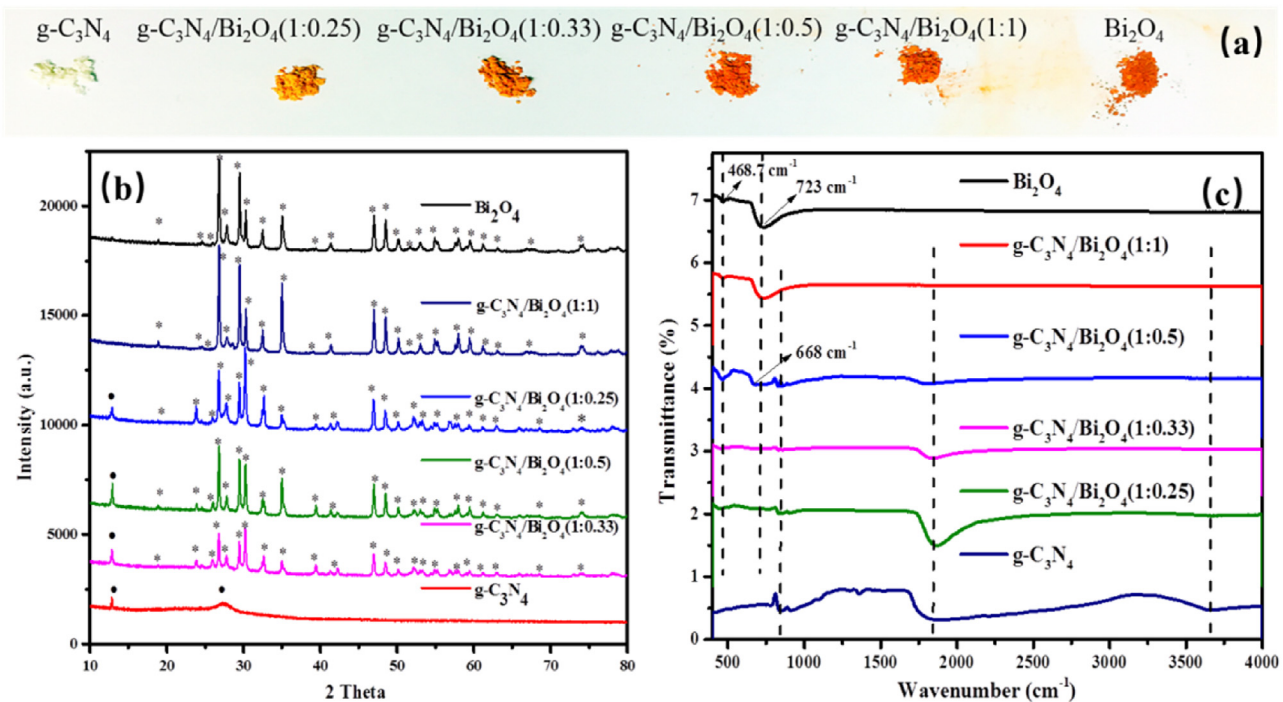


Fig. 1. (a) Photos of g-C₃N₄, g-C₃N₄/m-Bi₂O₄ and m-Bi₂O₄ powders showing the different colors, (b) XRD patterns and (c) FTIR spectrum of g-C₃N₄, g-C₃N₄/m-Bi₂O₄ and m-Bi₂O₄.

of •OH through measuring the spectrum on a fluorescence spectrophotometer at an excitation wavelength of 365 nm. H₂O₂ was analyzed based on the reaction of H₂O₂ with coumarin to form a high fluorescent compound named 7-hydroxylcoumarin, and was then measured on a fluorescence spectrophotometer with emission at 456 nm [33]. Electron paramagnetic resonance (EPR) spectra of •OH and •O₂[−] were recorded on a Bruker ElexsysE500 spectrometer by applying an X-band (9.43 GHz, 1.5 mW) microwave with sweeping magnetic field at 110 K in cells that can be connected to a conventional high-vacuum apparatus (residual pressure < 10^{−4} mbar).

2.6. Fourier transform infrared (FT-IR) spectroscopy

Samples were prepared by the following procedure: the suspensions at different reaction times were evaporated by a freeze-drying method, then the dry residue was supported on KBr pellets for FTIR measurement. A FTS-4000 Varian Excalibur Series FTIR spectrometer with attenuated total reflection (ATR) (Varian, USA) was used to collect the infrared spectra. Spectra from 4000 to 800 cm^{−1} were collected with a resolution of 4 cm^{−1}, and the ordinate was expressed as absorbance. Each spectrum was an average of 256 scans with automatic baseline correction.

3. Results and discussion

3.1. Structural and optical characterizations of g-C₃N₄/m-Bi₂O₄ hybrid photocatalyst

After the synthesis of pure g-C₃N₄, m-Bi₂O₄ and g-C₃N₄/m-Bi₂O₄, it is obvious to find that the modification with increasing m-Bi₂O₄ content changes the color of g-C₃N₄ from light yellow to red (Fig. 1a), implying increased absorption in visible light. As shown in the XRD patterns (Fig. 1b), g-C₃N₄ sample shows its characterization peaks at 27.4° and 13.0°, which can be indexed to the (002) and (100) diffraction plane of the graphite-like carbon nitride

(JCPDS-501250) [16]. Pure m-Bi₂O₄ exhibits identical diffraction peaks to the monoclinic phase of m-Bi₂O₄ (JCPDS-830410) [21]. The main characteristic diffraction peaks of g-C₃N₄/m-Bi₂O₄ hybrid materials did not change significantly after m-Bi₂O₄ hybridized with g-C₃N₄, confirming the co-existence of g-C₃N₄ and m-Bi₂O₄ in the g-C₃N₄/m-Bi₂O₄ hybrid materials. With the increase of m-Bi₂O₄ concentration, the intensity of diffraction peaks of m-Bi₂O₄ increase gradually at the expense of g-C₃N₄ peaks, reflecting their contents in the g-C₃N₄/m-Bi₂O₄ hybrids. Moreover, the XRD patterns of all the composites are well corresponding to Bi₂O₄ or g-C₃N₄, respectively, indicating there are no impurities formed in the composites.

The FT-IR spectra of g-C₃N₄, m-Bi₂O₄, and g-C₃N₄/m-Bi₂O₄ samples are shown in Fig. 1c. Pure g-C₃N₄ exhibits several strong characteristic peaks in the range of 1600–2000 1/cm, which can be ascribed to the typical stretching vibration of C–N heterocycles. The broad peaks at 3500–3700 1/cm can be assigned to the stretching vibration mode of H–N and C–H [34]. In addition, the sharp peak at 810 1/cm is the breathing mode of triazine units [34]. For pure m-Bi₂O₄, 468.7 and 723 1/cm is assigned as the symmetric stretching vibration peak of the Bi–O band in the m-Bi₂O₄ structure [16]. Especially, the FT-IR spectra of g-C₃N₄/m-Bi₂O₄ composites exhibit an overlap of both g-C₃N₄ and m-Bi₂O₄. The intensity of the peak at 468.7 and 723 1/cm increases with an increase of m-Bi₂O₄ content, and a little shift (about 5 1/cm) of the two IR peaks in the g-C₃N₄/m-Bi₂O₄ hybrids can be observed. The shifts of these functional groups indicate the chemical interaction and formation of cross-linked connections and covalent bonds, strengthening their chemical interaction between g-C₃N₄ and m-Bi₂O₄.

Fig. 2a–f show the SEM images of the as-prepared photocatalysts. Pure g-C₃N₄ polymer is an aggregation of many wrinkled sheets with irregular shapes (Fig. 2a), while m-Bi₂O₄ exhibits as nanorods with a diameter of ca. 2–5 μ m (Fig. 2f). As for g-C₃N₄/m-Bi₂O₄ composites, a few m-Bi₂O₄ nanorods are coated on the surface of g-C₃N₄, likely due to the rolling of lamellar g-C₃N₄ driven by the surface tension. Moreover, the EDX patterns (Fig. 2g) con-

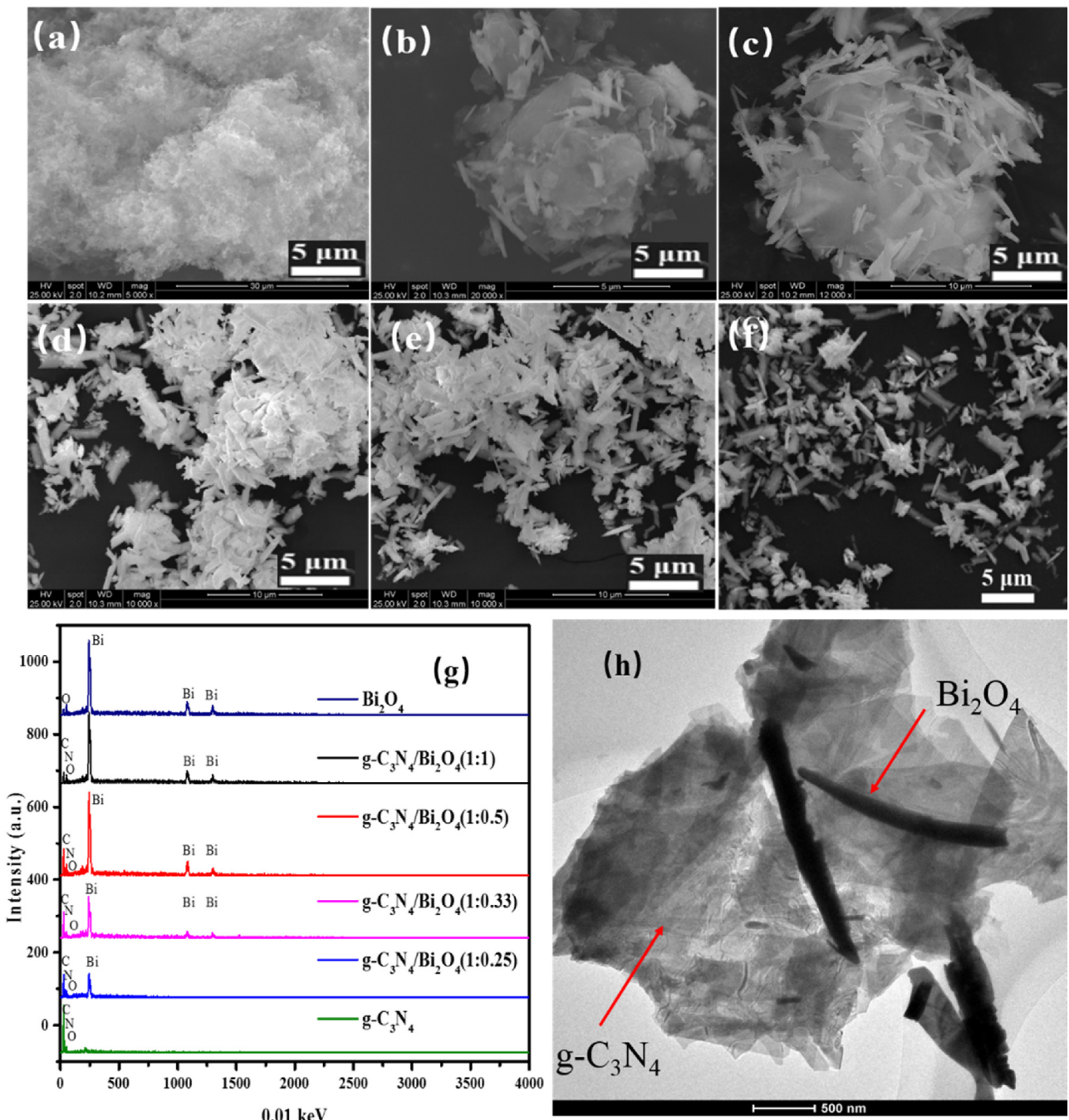


Fig. 2. SEM images of pure $\text{g-C}_3\text{N}_4$ (a), $\text{g-C}_3\text{N}_4/\text{m-Bi}_2\text{O}_4(1:0.25)$ (b), $\text{g-C}_3\text{N}_4/\text{m-Bi}_2\text{O}_4(1:0.33)$ (c), $\text{g-C}_3\text{N}_4/\text{m-Bi}_2\text{O}_4(1:0.5)$ (d), $\text{g-C}_3\text{N}_4/\text{m-Bi}_2\text{O}_4(1:1)$ (e), and pure $\text{m-Bi}_2\text{O}_4$ (f), EDX spectra (g), and TEM images (h) of $\text{g-C}_3\text{N}_4$, $\text{g-C}_3\text{N}_4/\text{m-Bi}_2\text{O}_4(1:0.5)$ and $\text{m-Bi}_2\text{O}_4$.

firm that the $\text{g-C}_3\text{N}_4/\text{m-Bi}_2\text{O}_4$ composites not only contain C, N, and O, but also Bi elements, in which Bi contents were increased with an increase of $\text{m-Bi}_2\text{O}_4$ contents. TEM images further verify that the sample consists of micron-sized $\text{m-Bi}_2\text{O}_4$ rods wrapped with lamellar texture of $\text{g-C}_3\text{N}_4$ (Figs. 2 h and S2).

XPS was further employed to investigate the surface chemical composition and chemical states of the $\text{g-C}_3\text{N}_4$, $\text{m-Bi}_2\text{O}_4$ and $\text{g-C}_3\text{N}_4/\text{m-Bi}_2\text{O}_4$ samples, wherein carbon, nitrogen, bismuth and oxygen species were detected (Fig. 3a). Fig. 3b shows the two peaks at 284.6 and 288.1 eV of C 1s spectra, which can be respectively attributed to the C and the N–C=N coordination in pure $\text{g-C}_3\text{N}_4$ and $\text{g-C}_3\text{N}_4/\text{m-Bi}_2\text{O}_4$ [35]. Especially, the intensity of C 1s peaks at 284.6 eV in $\text{g-C}_3\text{N}_4/\text{m-Bi}_2\text{O}_4$ was higher than that of pure $\text{g-C}_3\text{N}_4$.

C_3N_4 , indicating the $\text{m-Bi}_2\text{O}_4$ hybridized with $\text{g-C}_3\text{N}_4$ could result in inner shift of C 1s orbit. The N1s spectra of $\text{g-C}_3\text{N}_4$ and $\text{g-C}_3\text{N}_4/\text{m-Bi}_2\text{O}_4$ in Fig. 3c can be deconvoluted into three peaks, which are ascribed to sp² hybridized aromatic N bonded to carbon atom (C=N–C, 398.5 eV), tertiary N bonded to carbon atom (C–N)3, 399.8 eV) and quaternary N bonded three carbon atoms (N–(C)3, 401.3 eV) in the aromatic cycles, respectively [36]. Especially, there is a weakest peak at 404.3 eV (π -excitations) of N only observed in pure $\text{g-C}_3\text{N}_4$ rather than $\text{g-C}_3\text{N}_4/\text{m-Bi}_2\text{O}_4$. It implies that $\text{m-Bi}_2\text{O}_4$ covered up the π -excitations and coupled with $\text{g-C}_3\text{N}_4$ via an interaction using π -electrons of CN heterocycles, rather than coupled with sole C or N atoms of $\text{g-C}_3\text{N}_4$ [37]. The O1s spectra of $\text{g-C}_3\text{N}_4/\text{m-Bi}_2\text{O}_4$ and $\text{m-Bi}_2\text{O}_4$ were shown in Fig. 3d. For

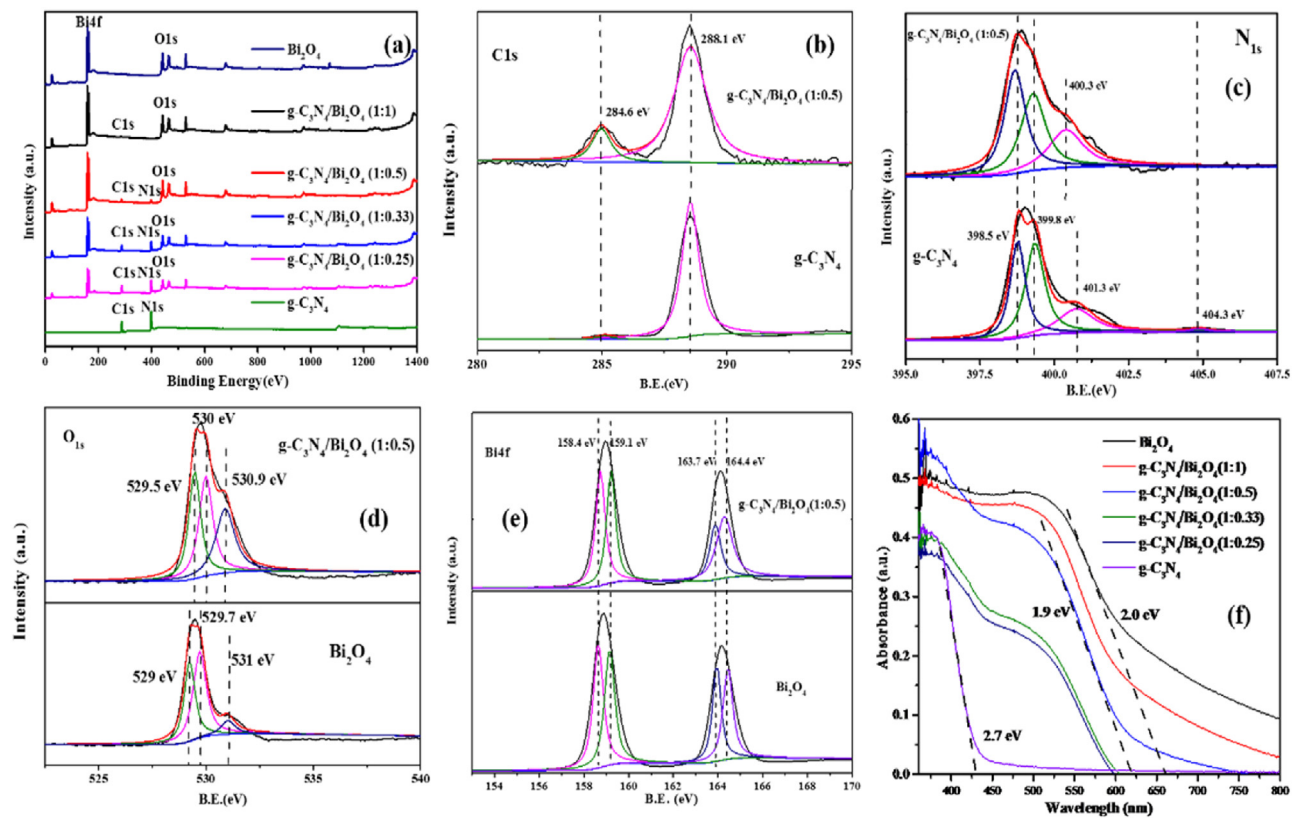


Fig. 3. (a) XPS spectra of m-Bi₂O₄, g-C₃N₄/m-Bi₂O₄ and g-C₃N₄, High-resolution XPS spectra of (b) C1s, (c) N 1s, (d) O 1s, and (e) Bi 4f of m-Bi₂O₄, g-C₃N₄/m-Bi₂O₄ (1:0.5) and g-C₃N₄, (f) UV-vis absorption spectra of g-C₃N₄, g-C₃N₄/m-Bi₂O₄ (1:0.5) and m-Bi₂O₄.

pure m-Bi₂O₄, 529.9 and 531.0 eV was attributed to crystal lattice O atoms (Bi-O) and surface OH, respectively [16,27]. The coupling of g-C₃N₄ and m-Bi₂O₄ resulted in a higher binding energy of crystal lattice O at 529.9 eV, indicating the coupling happened at O atoms for m-Bi₂O₄. Actually, m-Bi₂O₄ mainly contains terminal O atoms in its crystal structure. It indicates that the m-Bi₂O₄ is coupled to g-C₃N₄ via O-bridging. Fig. 3e displays the Bi4f spectra of m-Bi₂O₄ and g-C₃N₄/m-Bi₂O₄, the strong peaks of Bi4f_{7/2} (or 4f_{5/2}) can be deconvoluted well into two bimodal peaks at binding energy of 158.4 and 159.1 eV (or at 163.7 and 164.4 eV), which represent Bi(III) and Bi(V) of m-Bi₂O₄ [16,27]. Especially, the binding energies of the Bi peaks in g-C₃N₄/m-Bi₂O₄ are a little higher than pure m-Bi₂O₄, such results could be similarly attributed to the interaction of g-C₃N₄ with m-Bi₂O₄, resulting in inner shift of Bi 4f orbitals. All the observed shifts for binding energy in the XPS spectra can be attributed to the intense interaction of g-C₃N₄ and m-Bi₂O₄, further confirming the successful formation of the heterojunctions.

Fig. 3f shows the UV-vis DRS of g-C₃N₄, m-Bi₂O₄, and g-C₃N₄/m-Bi₂O₄. Modification of m-Bi₂O₄ extended the absorption edge of g-C₃N₄ in the visible light region, as evidenced by the emerging absorption bands red-shifts regularly from 430 nm to 655 nm with increasing of m-Bi₂O₄ content. The increased visible light absorption for g-C₃N₄/m-Bi₂O₄ suggests that the intermolecular interaction occurs between g-C₃N₄ and m-Bi₂O₄, thereby a narrowed bandgap obtained in hybrid g-C₃N₄/m-Bi₂O₄. The estimated bandgaps for pure Bi₂O₄ (2.0 eV) and g-C₃N₄ (2.7 eV) agree well with the reported references [27,38], whereas the calculated band gap of g-C₃N₄/m-Bi₂O₄ (1:0.5) is 2.3 eV. In conclusion, all the characterization results of g-C₃N₄/Bi₂O₄ hybrid nanocomposites suggest the effective assembly of m-Bi₂O₄ nanorods on g-C₃N₄ nanosheets, as well as the successful synthesis of g-C₃N₄/m-Bi₂O₄ nanocomposites.

3.2. Photocatalytic inactivation of *E. coli*

The *E. coli* inactivation performance was used to evaluate the visible light driven photocatalytic activity of as-prepared photocatalysts. As Fig. 4a shows, within 2-h light irradiation, a 4-log₁₀ cfu/mL reduction in *E. coli* population in the presence of pure m-Bi₂O₄ was achieved, and an approximately 1.5-log₁₀ cfu/mL reduction of *E. coli* was obtained when pure g-C₃N₄ was present. Fortunately, all g-C₃N₄/Bi₂O₄ samples demonstrate an enhanced photocatalytic inactivation activity than both pure photocatalysts. With the increase of m-Bi₂O₄ contents in g-C₃N₄/m-Bi₂O₄ from 1:0.25 to 1:0.5, an improvement of *E. coli* inactivation efficiency was obtained, which may be explained by the increased formation of heterojunctions between g-C₃N₄ and Bi₂O₄ in the composites. The highest photocatalytic inactivation activity was achieved with the g-C₃N₄/Bi₂O₄ (1:0.5), which could completely inactivate 6-log₁₀ cfu/mL *E. coli* within 1.5 h. As shown in Fig. S3, the performance was superior to the well documented BiOBr (2.5 h) and comparable to that of N-TiO₂, as the time for total inactivation of 6-log *E. coli* by BiOBr and N-TiO₂ were 2.5 h and 1.5 h, respectively. However, further increasing the ratio of g-C₃N₄/m-Bi₂O₄ to 1:1, a decreased photocatalytic inactivation performance was observed (1.75 h was needed for total inactivation of 6-log₁₀ cfu/mL *E. coli*). When the m-Bi₂O₄ contents were too high, the efficient heterojunction interface did not increase distinctly, whereas the excessive m-Bi₂O₄ with narrow band gap would act as the recombination center of photo-generated electrons and holes. Thus, the drop of the productivity should be ascribed to the decreasing the separation efficiency of electron-hole pairs. To further investigate the effect of the g-C₃N₄ modification and confirm the above-proposed mechanisms, the photoluminescence (PL) spectra of g-C₃N₄/m-Bi₂O₄ were obtained. PL spectra reveal the migration, transfer, and recombination pro-

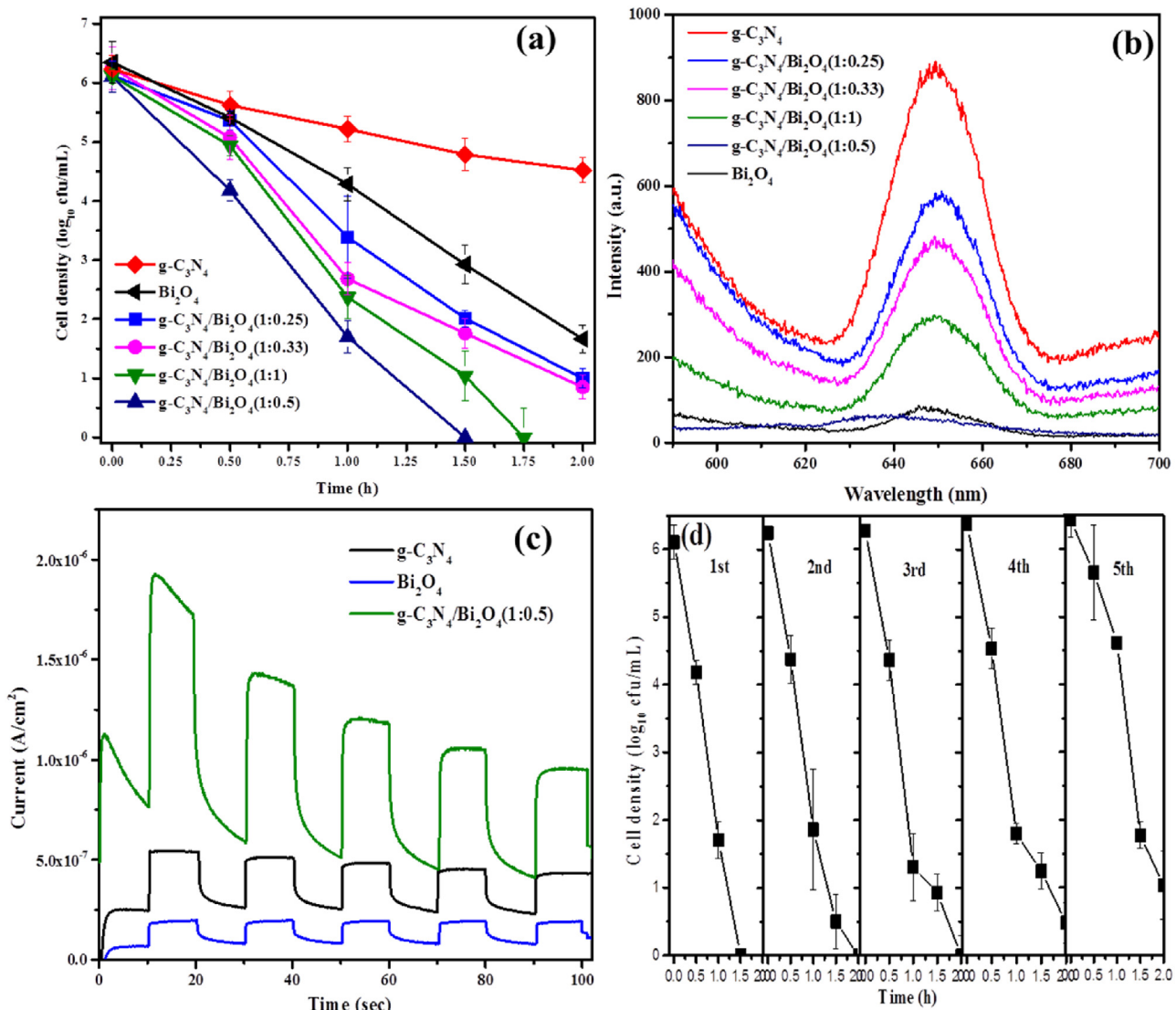


Fig. 4. (a) Photocatalytic inactivation of *E. coli* K-12 by m- Bi_2O_4 , $\text{g-C}_3\text{N}_4$ /m- Bi_2O_4 and $\text{g-C}_3\text{N}_4$; (b) Photoluminescence spectra of m- Bi_2O_4 , $\text{g-C}_3\text{N}_4$ /m- Bi_2O_4 and $\text{g-C}_3\text{N}_4$; (c) Photocurrent of m- Bi_2O_4 , $\text{g-C}_3\text{N}_4$ /m- Bi_2O_4 (1:0.5) and $\text{g-C}_3\text{N}_4$; (d) Repeated testing of the photocatalytic inactivation of *E. coli* K-12 over $\text{g-C}_3\text{N}_4$ /m- Bi_2O_4 (1:0.5). Experimental conditions: $[\text{E. coli K-12}] = 6 \log_{10}$ cfu/mL, [catalyst] = 0.4 g/L.

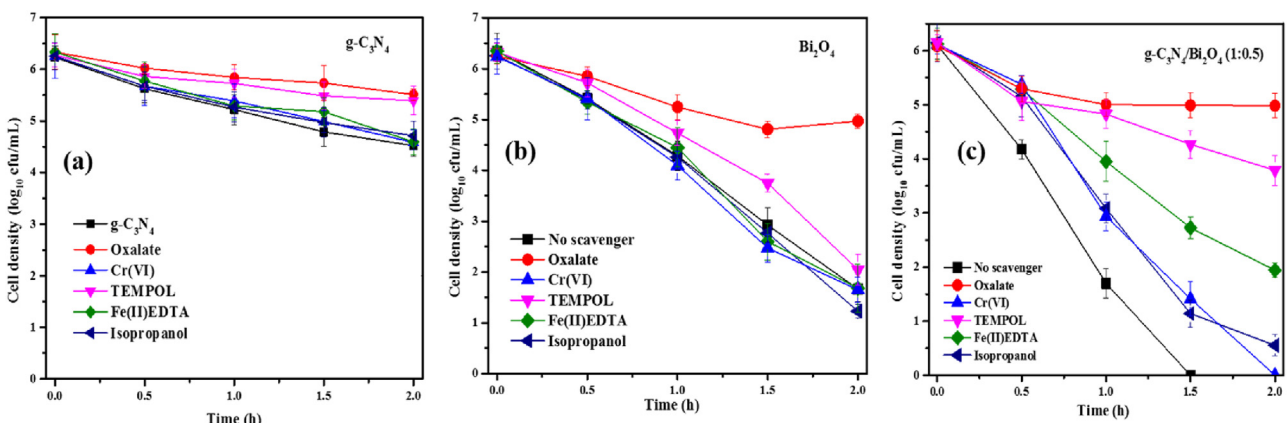


Fig. 5. Photocatalytic inactivation of *E. coli* K-12 with different scavengers by (a) $\text{g-C}_3\text{N}_4$, (b) $\text{m-Bi}_2\text{O}_4$, and (c) $\text{g-C}_3\text{N}_4$ /m- Bi_2O_4 (1:0.5) within 2 h visible light irradiation. Experimental conditions: $[\text{E. coli K-12}] = 6 \log_{10}$ cfu/mL, [catalyst] = 0.4 g/L.

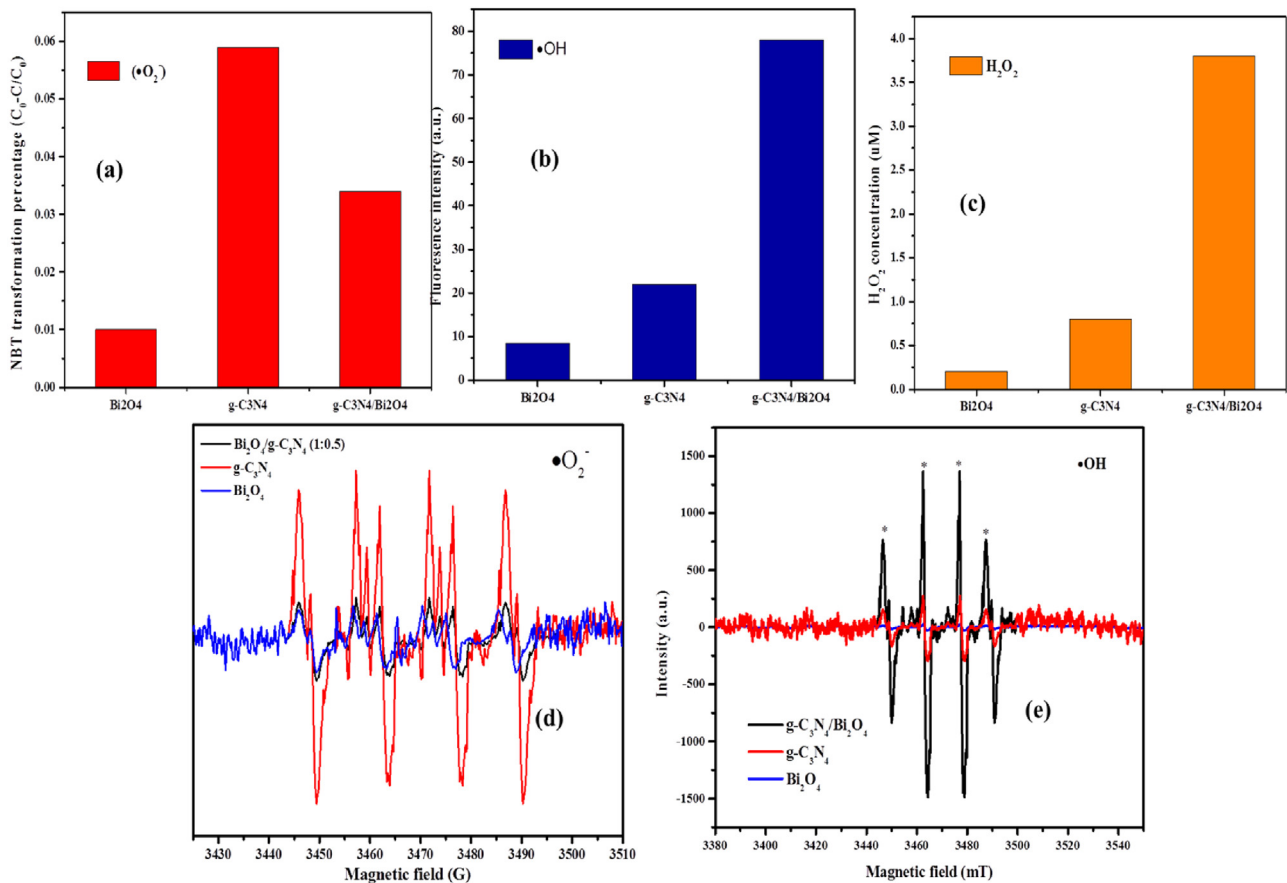


Fig. 6. (a) Transformation percentage of NBT concentration (b) Fluorescent intensity of TAOH (c) H_2O_2 concentration (d) DMPO spin-trapping ESR spectra recorded for $\bullet O_2^-$ and (e) $\bullet OH$ where the concentration of DMPO was 25 mM when g-C₃N₄, m-Bi₂O₄, and g-C₃N₄/m-Bi₂O₄(1:0.5) were irradiated within 2 h visible light irradiation.

cesses of photo-generated electron-hole pairs in semiconductors [39]. Fig. 4b presents the PL spectra of the g-C₃N₄/m-Bi₂O₄ composite photocatalysts at an excitation wavelength of 365 nm. At room temperature, the emission band for pure g-C₃N₄ was centered at 650 nm, which was attributed to the radiative recombination process of self-trapped excitations. The positions of the g-C₃N₄/m-Bi₂O₄ emission peaks were similar to pure g-C₃N₄. However, the emission intensity of the g-C₃N₄/m-Bi₂O₄ composite significantly decreased, with the g-C₃N₄/m-Bi₂O₄ (1:0.5) sample having the weakest intensity. This result clearly indicated that the recombination of photo-generated charge carriers was inhibited in the g-C₃N₄/m-Bi₂O₄ (1:0.5). The same results were obtained using a transient photocurrent responses experiment. As shown in Fig. 4c, although all three samples show a quick response to the light either on or off, the generated transient photocurrent is different. Under light irradiation, the generated photocurrent on the g-C₃N₄/m-Bi₂O₄ (1:0.5) electrode reaches 2 μA , which is four times and eight times higher than g-C₃N₄ and m-Bi₂O₄, respectively. This further demonstrates that g-C₃N₄/m-Bi₂O₄ (1:0.5) is superior to g-C₃N₄ and m-Bi₂O₄ in separating electron-hole pairs.

It was reported that photo-corrosion may occur after light irradiation, causing the deactivation of photocatalysts [40]. Therefore, the stability and recyclability of g-C₃N₄/m-Bi₂O₄ (1:0.5) were examined. The results evidenced that the activity of g-C₃N₄/m-Bi₂O₄ (1:0.5) did not decline significantly (5-log₁₀ cfu/mL of *E. coli* inactivation) after five cycles of *E. coli* inactivation under the visible light irradiation (Fig. 4d). Fortunately, XRD patterns (Fig. S4) also illustrate that the crystal structure of the g-C₃N₄/m-Bi₂O₄ (1:0.5) did not change after the photocatalytic reaction, confirming that

g-C₃N₄/m-Bi₂O₄ (1:0.5) can be evaluated as a stable photocatalyst for bacterial inactivation without photo-corrosion.

3.3. Investigation of reactive species

Generally, the photocatalytic bacterial inactivation involves the surface reactions of both photogenerated holes and electrons, which may also produce reactive oxygen species, such as $\bullet O_2^-$, $\bullet OH$ and H_2O_2 to further accelerate the oxidation reactions [41]. The reactive species trapping experiments were employed to investigate the main active species in the photocatalytic *E. coli* inactivation over the g-C₃N₄, m-Bi₂O₄, and g-C₃N₄/m-Bi₂O₄ (1:0.5), which was useful in deducing the charge transmission route in the hybrid composite photocatalyst [42]. As shown in Fig. 5, with addition of sodium oxalate (a hole scavenger), the *E. coli* inactivation was significantly depressed for g-C₃N₄, m-Bi₂O₄, and g-C₃N₄/m-Bi₂O₄ (1:0.5), suggesting that the photogenerated holes played a critical role in *E. coli* inactivation in the three cases. On the other hand, when Cr(VI) (an electron scavenger) was added, the *E. coli* inactivation was inhibited over the three photocatalysts, implying that photo-generated electrons were indispensable for directly attack *E. coli* for the three cases.

Considering the fact that conduction band electrons can be captured by O_2 to produce reactive oxygen species, it is essential to explore the role of these species in *E. coli* inactivation. As shown in Fig. 5, addition of TEMPOL (a $\bullet O_2^-$ scavenger) clearly depressed the *E. coli* inactivation rate on g-C₃N₄ (Fig. 5a) and g-C₃N₄/m-Bi₂O₄ (1:0.5) (Fig. 5c), but not for m-Bi₂O₄ (Fig. 5b), implying different roles of $\bullet O_2^-$ in the three systems. Fig. 5 shows that the addition of Fe(II)-EDTA (a H_2O_2 scavenger) did not affect the *E. coli* rate over

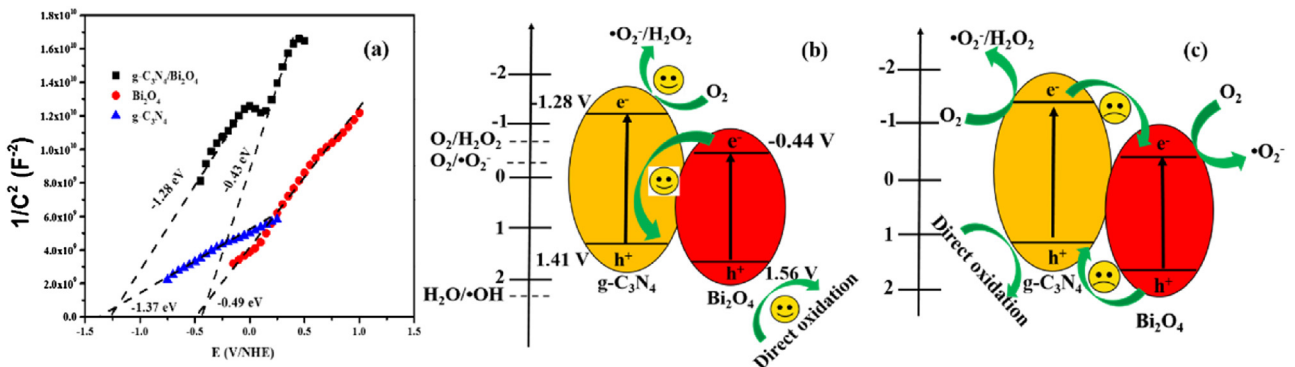
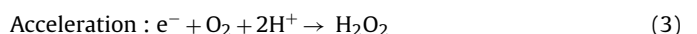


Fig. 7. (a) Mott–Schottky plots for g-C₃N₄, m-Bi₂O₄, g-C₃N₄/m-Bi₂O₄(1:0.5) at frequency obtained in darkness; Two models of charge separation proposed for g-C₃N₄/m-Bi₂O₄(1:0.5) under visible irradiation: (b) Conventional donor-acceptor charge transfer, and (c) Z-scheme electron transfer.

g-C₃N₄ and m-Bi₂O₄ but g-C₃N₄/m-Bi₂O₄ (1:0.5), indicating that H₂O₂ involves in the *E. coli* inactivation by g-C₃N₄/m-Bi₂O₄ (1:0.5). Moreover, the addition of isopropanol (a •OH scavenger) slightly inhibited the *E. coli* inactivation rate over g-C₃N₄/m-Bi₂O₄ (1:0.5), whereas no inhibition over g-C₃N₄ and m-Bi₂O₄, suggesting •OH plays a moderate role for g-C₃N₄/m-Bi₂O₄ (1:0.5) rather than g-C₃N₄ and m-Bi₂O₄. On the basis of these comparative observations, it is reasonable to conclude that the photogenerated hole, •O₂⁻ and H₂O₂ are indispensable, playing synergic roles in the *E. coli* inactivation over g-C₃N₄/Bi₂O₄ (1:0.5), whereas that of g-C₃N₄ are hole and •O₂⁻ and m-Bi₂O₄ are only hole. Obviously, the results indicate the coupling of m-Bi₂O₄ with g-C₃N₄ leads to the different photocatalytic mechanism.

To further analyze the roles of different reactive oxygen species in pure g-C₃N₄, pure m-Bi₂O₄ and g-C₃N₄/m-Bi₂O₄ (1:0.5), the detailed •O₂⁻, •OH and H₂O₂ semi-quantification experiments were used. Fig. 6a–c shows the transformation percentage of NBT (quantification experiments of •O₂⁻ production), the fluorescent intensity of TAOH (quantification experiments of •OH production), the concentration of H₂O₂ within 2-h visible light irradiation for the three photocatalysts, respectively [43]. For m-Bi₂O₄, the transformation percentage of NBT, the fluorescent intensity of TAOH, and the concentration of H₂O₂ are negligible, indicating there are limited •O₂⁻, •OH and H₂O₂ formation from the h⁺ or e⁻ of m-Bi₂O₄. The reason is shown as following: the conduction band (CB) potential of m-Bi₂O₄ (-0.37 eV vs NHE) is similar with the standard potential of E₀(O₂/•O₂⁻ = -0.33 eV vs NHE), and the standard redox potential of Bi⁴⁺/Bi³⁺ (1.59 eV) is more negative than that of •OH/OH⁻ (+1.99 eV), thereby only limited reactive oxygen species can be thermodynamically generated [27]. For g-C₃N₄, the CB potential of g-C₃N₄ (-1.28 eV) is more negative than E₀(O₂/•O₂⁻ = -0.33 eV vs NHE), thereby g-C₃N₄ shows obvious transformation percentage of NBT (Fig. 6a), indicating more generation of •O₂⁻ for g-C₃N₄ than m-Bi₂O₄. Theoretically, due to the VB potential (+1.57 eV vs NHE) of g-C₃N₄ is more negative than E₀ (•OH/OH⁻ = +1.99 eV vs NHE), the generation of •OH is thermodynamically forbidden from the h⁺ in VB of g-C₃N₄. However, the observed fluorescent intensity of TAOH was very high as shown in Fig. 6b, which reveals the •OH production of g-C₃N₄, consistent with previous report [44]. In fact, the •OH can also be produced from electrons in CB via a two-electron oxidation pathway (H₂O₂ → •OH), since in photocatalysis H₂O₂ can be normally generated through direct reduction (O₂ → H₂O₂, -1.18 eV vs NHE) or a multistep reaction (O₂ → •O₂⁻ → H₂O₂) from oxygen. Fortunately, a 0.75 μM H₂O₂ was detected in the g-C₃N₄ system, mainly generated from electron reduction pathway on the CB in Fig. 6c [45].

For the g-C₃N₄/m-Bi₂O₄ (1:0.5) composite, the fluorescent intensity of TAOH and concentration of H₂O₂ increased to 4 and 5 times, respectively, higher than that of the g-C₃N₄ system (Fig. 6b, 6c), indicating more photo-generated electrons survived in the CB of g-C₃N₄/m-Bi₂O₄ (1:0.5) and resulted in the increase formation of •OH and H₂O₂. However, a decreased transformation percentage of NBT (10.9%) was observed (Fig. 6a), suggesting the electrons in the CB of g-C₃N₄/m-Bi₂O₄ (1:0.5) reacted with O₂ to only produce less •O₂⁻ than pure g-C₃N₄. This result suggested that H₂O₂ was likely produced via direct reduction (O₂ → H₂O₂) in the g-C₃N₄/m-Bi₂O₄ (1:0.5) suspension, rather than the multistep reaction route (O₂ → •O₂⁻ → H₂O₂) in g-C₃N₄. To further confirm this observation, a DMPO spin-trapping ESR technique was employed to characterize the •O₂⁻ species generated during photocatalysis. As shown in Fig. 6d, four characteristic peaks of DMPO-•O₂⁻ were clearly observed in methanol suspensions of g-C₃N₄, whereas only a trace level of DMPO-•O₂⁻ could be detected for the g-C₃N₄/Bi₂O₄ (1:0.5) under the same conditions. Meanwhile, it was found the intensity of •OH signal was much higher in the composite than pure g-C₃N₄ and Bi₂O₄, further conforming more •OH generated by the composite (Fig. 6e). It is reasonable that more H₂O₂ generation will dissipate into higher concentration of •OH. Based on the above results, the process of photocatalytic *E. coli* inactivation over g-C₃N₄/Bi₂O₄ (1:0.5) involved Eqs. (1)–(5), in which the step 3 was accelerated.



3.4. Determination of the charge transfer mode

To further reveal the reduction and oxidation reactions occurring at the photocatalyst surface, the band energy alignment of the composites were determined by combining Mott–Schottky plots (Fig. 7a) and UV–vis DRS (Fig. 3f). Both g-C₃N₄ and m-Bi₂O₄ samples display n-type semiconductor characteristics. The flat-band potential (equal to CB band in n-type semiconductor) was measured at -1.37 V vs NHE for pure g-C₃N₄ and -1.28 V vs NHE for the g-C₃N₄ part in g-C₃N₄/Bi₂O₄. With the known band gap of 2.69 eV for g-C₃N₄ (Fig. 3f), the VB potential of g-C₃N₄ can be calculated to be 1.41 V in the g-C₃N₄/Bi₂O₄ composite. The second linear region in the Mott–Schottky plot of g-C₃N₄/m-Bi₂O₄ is attributed to the CB band of the m-Bi₂O₄ part, corresponding to a potential of -0.43 V for the m-Bi₂O₄ part in g-C₃N₄/Bi₂O₄. Similarly, with the known band gap of 2.0 V for m-Bi₂O₄ (Fig. 3f), the VB potential of m-Bi₂O₄

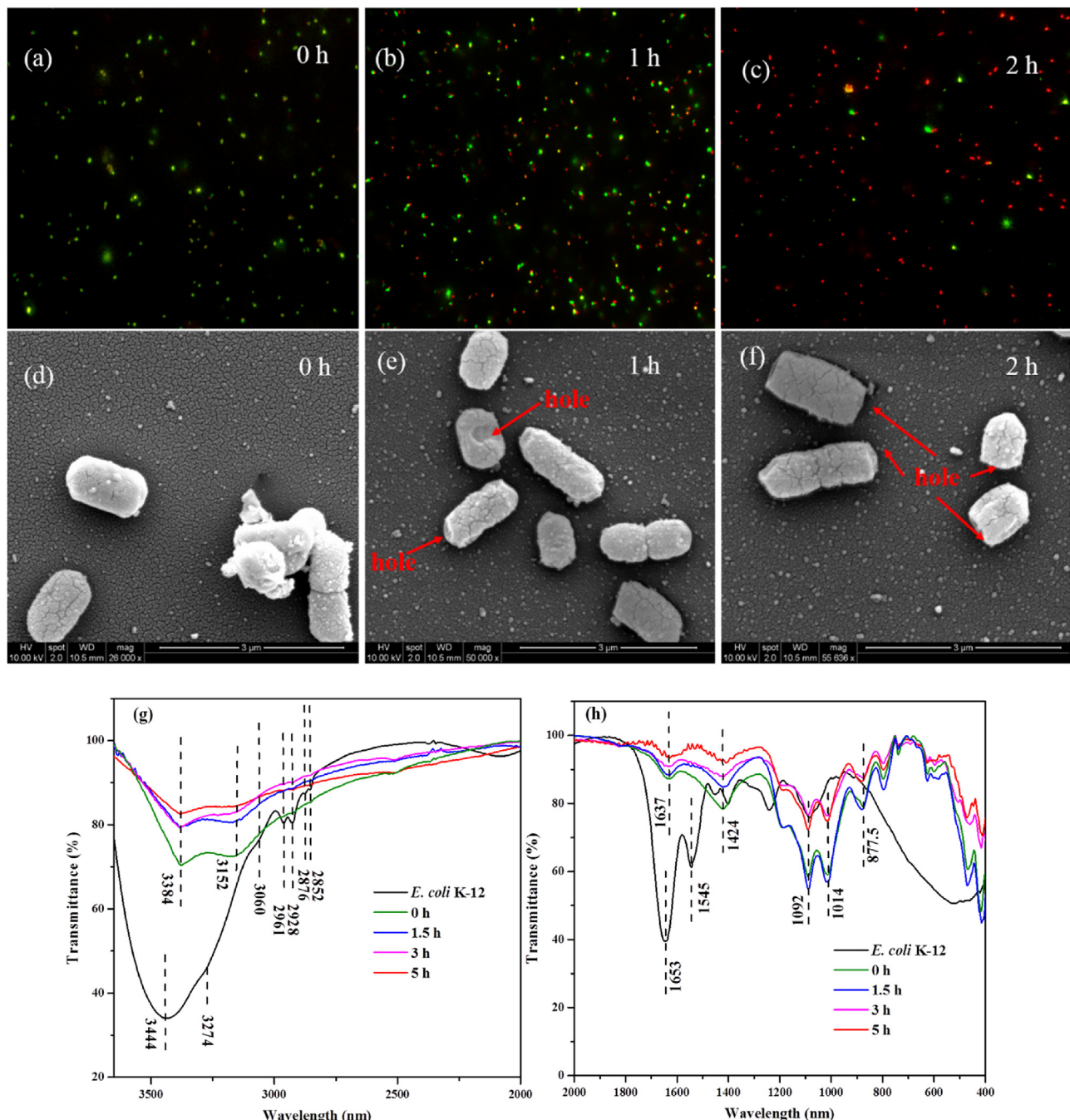


Fig. 8. Fluorescence microscopic images (a-c), SEM images (d-f) and FTIR (g-h) spectra of *E. coli* K-12 before and after photocatalytically treated with g-C₃N₄/m-Bi₂O₄. Experimental conditions: [E. coli K-12] = 6 log₁₀ cfu/mL, [catalyst] = 0.4 g/L.

can be calculated to be 1.57 V in the g-C₃N₄/m-Bi₂O₄ composite. For pure m-Bi₂O₄, the measured CB band is at -0.49 V and VB band is at 1.51 V, respectively.

The direction of the photogenerated charge across the heterojunctions for the synthesized materials can be inferred by coupling the experimental results with the established band alignment. In the present study, m-Bi₂O₄ was deposited on g-C₃N₄ surface and the hybrid junctions were formed at the interfacial phases, resulting in inner electrical fields established in the direction from g-C₃N₄ to m-Bi₂O₄. When exposing to the visible light, the VB electrons of both g-C₃N₄ and m-Bi₂O₄ could be excited up. The charge transfer at the interfacial phases may follow the Z-scheme transfer mode (Fig. 7b) or double-transfer mechanism (Fig. 7c). According to above

results in Fig. 6, the electron can enrich on the CB of g-C₃N₄ (thereby retaining sufficient capacity to reduce O₂ species to H₂O₂ and •OH), only when the electron and holes in g-C₃N₄/m-Bi₂O₄ (1:0.5) migrate by the Z-scheme mechanism. Otherwise, if the double-transfer mechanism is adopted, the photogenerated electron would accumulate on the CB of m-Bi₂O₄ and result in the dominant reactive species of •O₂⁻ rather than H₂O₂, which is inconsistent with the experimental result.

Under VL irradiation, both g-C₃N₄ and m-Bi₂O₄ were excited, and the photogenerated holes and electrons were in their VB and CB, respectively. Then, the internal static electric fields of m-Bi₂O₄ resulted in that the e⁻ of m-Bi₂O₄ transfer to the interface between g-C₃N₄ and m-Bi₂O₄. The electron located in the CB of g-C₃N₄ pos-

sessed higher reducing power (by -0.84 V in comparison to that of $\text{m-Bi}_2\text{O}_4$), thereby enabling direct reduction of O_2 to H_2O_2 and $\cdot\text{OH}$ (Eq. (3)), which was consistent with the results presented in Fig. 5 and 6. Meanwhile, the higher level of VB of $\text{m-Bi}_2\text{O}_4$ (by 1.71 V in comparison to that of $\text{g-C}_3\text{N}_4$) provided stronger oxidizing power for the hole, thus enabling direct oxidation of *E. coli* (Eq. (5)), which was consistent with the results shown in Fig. 5 and 6. The heterojunction charge separation as illustrated by the Z-scheme reduces the probability of charge recombination that is often encountered in the single-component photocatalyst, thus producing an increased density of holes and electrons for enhanced performance.

3.5. Bacterial destruction process

The processed bacterial membrane integrity was visually observed through fluorescence microscopy. As shown in Fig. 8a–c, after staining with a fluorescent dye mixture, the red fluorescent cells increased in number to replace the green fluorescent cells after prolonged treatment, indicating cell membrane rupture during photocatalytic process [46]. Meanwhile, the *E. coli* destruction process using the $\text{g-C}_3\text{N}_4/\text{m-Bi}_2\text{O}_4$ photocatalyst was also visually observed by SEM. Before treatment, the *E. coli* cell had an intact cell structure and a well preserved rod shape (Fig. 8d). During the inactivation process, the characteristic rod shape of the cell became abnormal, and the cell's shape was distorted with holes (Fig. 8e–f). This point to the fact that sustainably generated RSs can cause a myriad of adverse effects on the cell envelope. Actually, the cell envelope contains essential protein components such as respiratory chain, which generate energy (ATP) with functionalized electron chains, playing a vital role in bacterial metabolism. As Fig. S5a shows, associated with the damaged cell envelope, the cells were almost instantaneously inactivated by metabolic arrest as a consequence of a drastic drop in the ATP level, with ATP level decreased from $123.8\text{ RLU}/10^3$ to zero after the exposure to VL irradiated $\text{g-C}_3\text{N}_4/\text{m-Bi}_2\text{O}_4$ (1:0.5) within 1 h. The loss of ATP generation capacity directly caused bacterial death: a lack of ATP limits the cellular energy supply, preventing cellular repair and bacterial growth. Meanwhile, a remarkable decrease in both SOD and CAT activities was observed after 0.5 h and continued thereafter (Fig. S5b–c), further confirming that the defense capacity was overwhelmed by ROS at the initial stage and then decomposed rapidly. Damage to the anti-oxidative defense system will facilitate the ROS flood into cells and aggravate the oxidation of *E. coli*.

FTIR provides a means to identify key functional groups and structures of the cells, and evaluate changes of cells caused through exposure to oxidants [40]. In Fig. 8g, a wide skewed band in the region $3400\text{--}3600\text{ cm}^{-1}$ due to the OH^- vibrations of the absorbed water and OH^- on the catalyst surface. For *E. coli* cells alone, the characteristic peaks at 3274 and 3060 cm^{-1} were attributed to amide A and amide B, and the peaks at 2961 , 2928 , 2876 , and 2852 cm^{-1} were assigned to νa (CH_3), νa (CH_2), νs (CH_3), and νs (CH_2), respectively. With increasing experimental time to 3 h, the intensity and integral absorbance of these initial *E. coli* spectral profiles quickly shifted, disappeared or decayed. After 5 h, the disappearance of amide A (3274 cm^{-1}) and amide B (3060 cm^{-1}) were observed, and also the peak intensity of the C–H bands (2963 , 2927 , 2872 , and 2852 cm^{-1}) were almost undetectable. Concomitantly, the wide band containing OH^- vibrations is transformed to a skewed form with a maximum at around 3384 cm^{-1} . Similarly, Fig. 8h also exhibits significant decay of the PO_2^- band near 1242 cm^{-1} and oligosaccharide bands around $1014\text{--}1092\text{ cm}^{-1}$, as well as the amide I band near 1653 cm^{-1} and the amide II band near 1545 cm^{-1} after 5 h treatment. Based on above observations, the results revealed that the cell envelope of *E. coli* K-12 were

firstly decomposed, then cytoplasmic components leaked out and degraded, finally resulting in the cell death.

4. Conclusions

In summary, an all-solid-state Z-scheme heterojunction ($\text{g-C}_3\text{N}_4/\text{m-Bi}_2\text{O}_4$) has been successfully constructed. As tested for photocatalytic inactivation of *E. coli* under visible light, significant enhancement in photocatalytic activity was observed for $\text{g-C}_3\text{N}_4/\text{m-Bi}_2\text{O}_4$ (1:0.5) in comparison to the pristine $\text{g-C}_3\text{N}_4$ and $\text{m-Bi}_2\text{O}_4$. The Z-scheme heterojunction creates charge separation with the electron populated to the higher CB and hole to the lower VB, thus enhancing the redox reaction power of the charge carriers. The strong electron of $\text{g-C}_3\text{N}_4$ can trigger the direct reduction of O_2 to H_2O_2 , collectively work with the strong photogenerated holes of $\text{m-Bi}_2\text{O}_4$ to attack *E. coli*. This study provides new insights into the rational design of effective photocatalysts that can be operated under visible light, particularly for purifying hospital wastewater contaminated with highly concentrated pathogenic microorganisms.

Acknowledgement

The project was supported by a research grant (GRF14100115) of the Research Grant Council, Hong Kong SAR Government and the Technology and Business Development Fund (TBF15SCI008) of The Chinese University of Hong Kong to P.K. Wong, and the research grants (21607028, 41603097, 41573086, and 41425015) of National Science Foundation of China to W.J. Wang, D.H. Xia, G.Y. Li, T.C. An, respectively. H.J. Zhao and P.K. Wong were also supported by CAS/SAFEA International Partnership Program for Creative Research Teams of Chinese Academy of Sciences (2015HSC-UE004).

Appendix A. Supplementary data

Supplementary data associated with this article can be found, in the online version, at <http://dx.doi.org/10.1016/j.apcatb.2017.05.035>.

References

- [1] D. Haaken, T. Dittmar, V. Schmalz, E. Worch, *Water Res.* 52 (2014) 20–28.
- [2] L.C. Rietveld, D. Norton-Brando, R. Shang, J. van Agtmaal, J.B. van Lier, *Water Sci. Technol.* 64 (2011) 1540–1546.
- [3] P.H. Dobrowsky, M. De Kwaadsteniet, T.E. Cloete, W. Khan, *Appl. Environ. Microbiol.* 80 (2014) 2307–2316.
- [4] J.A. Soller, M.E. Schoen, A. Varghese, A.M. Ichida, A.B. Boehm, S. Eftim, N.J. Ashbolt, J.E. Ravenscroft, *Water Res.* 66 (2014) 254–264.
- [5] A.C. Eischeid, J.A. Thurston, K.G. Linden, *Crit. Rev. Environ. Sci. Technol.* 41 (2011) 1375–1396.
- [6] E.M. Anastasi, T.D. Wohlsen, H.M. Stratton, M. Katouli, *Water Res.* 47 (2013) 6670–6679.
- [7] AWWA, *Water Treatment: Principles and Practices of Water Supply Operations*, American Water Works Association, Denver, 1995.
- [8] K.M. Parker, T. Zeng, J. Harkness, A. Vengosh, W.A. Mitch, *Environ. Sci. Technol.* 48 (2014) 11161–11169.
- [9] V.K. Sharma, R. Zboril, T.J. McDonald, *J. Environ. Sci. Health B* 49 (2014) 212–228.
- [10] H. Sun, G. Li, X. Nie, H. Shi, P.K. Wong, H.J. Zhao, T. An, *Environ. Sci. Technol.* 48 (2014) 9412–9419.
- [11] L. Xiong, T.W. Ng, Y. Yu, D. Xia, H.Y. Yip, G. Li, T. An, H.J. Zhao, P.K. Wong, *Electrochim. Acta* 153 (2015) 583–593.
- [12] A. Kubacka, M.S. Diez, D. Rojo, R. Bargiela, S. Ciordia, I. Zapico, J.P. Albar, C. Barbas, V. dos Santos, M. Fernandez-Garcia, M. Ferrer, *Sci. Rep.* 4 (2014) 4134.
- [13] C. Ruales-Lonfat, N. Benitez, A. Sienkiewicz, C. Pulgarin, *Appl. Catal. B: Environ.* 160–161 (2014) 286–297.
- [14] C. Santella, B. Allainmat, F. Simonet, C. Chaneac, J. Labille, M. Auffan, J. Rose, W. Achouak, *Environ. Sci. Technol.* 48 (2014) 5245–5253.
- [15] T. An, J. An, Y. Gao, G. Li, H. Fang, W. Song, *Appl. Catal. B: Environ.* 164 (2015) 279–287.
- [16] D. Xia, M.C.I. Lo, *Water Res.* 100 (2016) 393–404.

- [17] X. Yang, C. Cao, L. Erickson, K. Hohn, R. Maghirang, K. Klabunde, *J. Catal.* 260 (2008) 128–133.
- [18] M. Xing, J. Zhang, F. Chen, *Appl. Catal. B: Environ.* 89 (2009) 563–569.
- [19] Z. Zhang, J. Long, L. Yang, W. Chen, W. Dai, X. Fu, X. Wang, *Chem. Sci.* 2 (2011) 1826–1830.
- [20] F. Su, S.C. Mathew, G. Lipner, X.Z. Fu, M. Antonietti, S. Blechert, X. Wang, *J. Am. Chem. Soc.* 132 (2010) 16299–16301.
- [21] X. Wang, K. Maeda, A. Thomas, K. Takanabe, G. Xin, J.M. Carlsson, K. Domen, M. Antonietti, *Nat. Mater.* 8 (2009) 76–80.
- [22] Y. Zhang, T. Mori, J. Ye, M. Antonietti, *J. Am. Chem. Soc.* 132 (2010) 6294–6295.
- [23] J. Zhang, G. Zhang, X. Chen, S. Lin, L. Mohlmann, G. Dolega, G. Lipner, M. Antonietti, S. Blechert, X. Wang, *Angew. Chem. Int. Ed.* 51 (2012) 3183–3187.
- [24] J. Huang, W.K. Ho, X. Wang, *Chem. Commun.* 50 (2014) 4338–4340.
- [25] Y. He, L. Zhang, B. Teng, M. Fan, *Environ. Sci. Technol.* 49 (2015) 649–656.
- [26] L. Ye, J. Liu, Z. Jiang, T. Peng, L. Zan, *Appl. Catal. B: Environ.* 142–143 (2013) 1–7.
- [27] P. Zhou, J.G. Yu, M. Jaroniec, *Adv. Mater.* 26 (2014) 4920–4935.
- [28] G. Dong, L. Yang, F. Wang, L. Zang, C. Wang, *ACS Catal.* 6 (2016) 6511–6519.
- [29] W. Wang, X. Chen, G. Liu, Z. Shen, D. Xia, P.K. Wong, J.C. Yu, *Appl. Catal. B: Environ.* 176–177 (2015) 444–453.
- [30] Y. He, L. Zhang, B. Teng, M. Fan, *Environ. Sci. Technol.* 49 (2015) 649–656.
- [31] D. Wu, B. Wang, W. Wang, T. An, G. Li, T.W. Ng, H.Y. Yip, C. Xiong, P.K. Wong, J. Mater. Chem. A 3 (2016) 15148–15155.
- [32] C. Di Valentin, E. Finazzi, G. Pacchioni, A. Selloni, S. Livraghi, M.C. Paganini, E. Giamello, *Chem. Phys.* 339 (2007) 44–56.
- [33] D. Xia, Z. Shen, G. Huang, W. Wang, J.C. Yu, P.K. Wong, *Environ. Sci. Technol.* 49 (2015) 6264–6273.
- [34] S. Chen, P. Slattum, C.Y. Wang, L. Zang, *Chem. Rev.* 115 (2015) 11967–11998.
- [35] Y. Wang, R. Shi, J. Lin, Y. Zhu, *Energy Environ. Sci.* 4 (2011) 2922–2929.
- [36] L. Qi, J. Yu, M. Jaroniec, *Phys. Chem. Chem. Phys.* 13 (2011) 8915–8923.
- [37] A. Thomas, A. Fischer, F. Goettmann, M. Antonietti, J.-O. Mueller, R. Schloegl, J.M. Carlsson, *J. Mater. Chem.* 18 (2008) 4893–4908.
- [38] S. Wang, D. Li, C. Sun, S. Yang, Y. Guan, H. He, *Appl. Catal. B: Environ.* 144 (2014) 885–892.
- [39] H. Cheng, J. Hou, O. Takeda, X. Guo, H. Zhu, *J. Mater. Chem. A* 3 (2015) 11006–11013.
- [40] D. Xia, T.W. Ng, T. An, G. Li, Y. Li, H.Y. Yip, H. Zhao, A. Lu, P.K. Wong, *Environ. Sci. Technol.* 47 (2013) 11166–11173.
- [41] F. Dong, Z. Wang, Y. Li, W.K. Ho, S.C. Lee, *Environ. Sci. Technol.* 48 (2014) 10345–10353.
- [42] G. Li, X. Nie, J. Chen, Q. Jiang, T. An, P.K. Wong, H. Zhang, H. Zhao, H. Yamashita, *Water Res.* 86 (2015) 17–24.
- [43] D. Xia, T. An, G. Li, W. Wang, H.J. Zhao, P.K. Wong, *Water Res.* 99 (2016) 149–161.
- [44] S. Li, G. Dong, R. Hailili, L. Yang, Y. Li, F. Wang, Y. Zeng, C. Wang, *Appl. Catal. B: Environ.* 190 (2016) 26–35.
- [45] L. Wang, M. Cao, Z. Ai, L. Zhang, *Environ. Sci. Technol.* 48 (2014) 3354–3362.
- [46] L. Zhang, K.H. Wong, H.Y. Yip, C. Hu, J.C. Yu, C.Y. Chan, P.K. Wong, *Environ. Sci. Technol.* 44 (2010) 1392–1398.